Journal of Applied Meteorology and Climatology

Another Look at the Refractive Index Structure Function

--Manuscript Draft--

Manuscript Number:	JAMC-D-11-0263
Full Title:	Another Look at the Refractive Index Structure Function
Article Type:	Article
Abstract:	This paper provides a review of the derivation of the refractive index structure function. It shows that the traditional formulation, based on the hydrostatic assumption, leads to increasing errors with height when compared with a formulation based on the potential temperature. The new derivation may have applications in observational work to measure Cn2 and seeing and in numerical modeling efforts. Analysis of the influence of the new formulation in numerical modeling of seeing suggests that impact will be small because the largest contribution to seeing generally comes from the lower troposphere. Secondly, model calibration algorithms can be formulated to take the difference in formulation into account. Nevertheless, under conditions of significant wind shear aloft the new formulation is likely to provide superior results.

Another Look at the Refractive Index Structure Function

T. Cherubini and S. Businger

University of Hawaii

Submitted to Journal of Applied Meteorology and Climatology

December 2011

Abstract

This paper provides a review of the derivation of the refractive index structure function. It shows that the traditional formulation, based on the hydrostatic assumption, leads to increasing errors with height when compared with a formulation based on the potential temperature. The new derivation may have applications in observational work to measure C_n^2 and seeing and in numerical modeling efforts. Analysis of the influence of the new formulation in numerical modeling of seeing suggests that impact will be small because the largest contribution to seeing generally comes from the lower troposphere. Secondly, model calibration algorithms can be formulated to take the difference in formulation into account. Nevertheless, under conditions of significant wind shear aloft the new formulation is likely to provide superior results.

1. Introduction

The physical origin of the optical effects of atmospheric turbulence is in the random index-of-refraction fluctuations, also known as optical turbulence. The energy source for optical turbulence is derived from larger scale wind shear or convection. Because an analytic solution of the equations of motion is not possible for turbulent flow, statistical treatments are used.

In general, turbulent flow in the atmosphere is neither homogeneous nor isotropic. However, it can be considered locally homogeneous and isotropic in small sub-regions of the atmosphere. These regions are those whose scale lies between that of the larger eddies that comprise the energy source for the turbulence and the small scale eddies for which viscous effects become important. This region of locally isotropic turbulence is know as the inertial subrange (Fig. 1).

The fundamental statistical description of atmospheric turbulence in the inertial subrange was developed by Kolmogorov (1941) in terms of velocity field fluctuations. Kolmogorov assumed that the velocity fluctuations can be represented by a locally homogeneous and isotropic random field for scales smaller than the large eddies that provide the energy source for the turbulence. This implies that the second and higher order statistical moments of the turbulence depend only on the distance between any two points in the turbulent layer.

Using dimensional analysis, Kolmogorov showed that the structure function of the velocity field in the inerial sub-range satisfies a universal 2/3 power law. The turbulent fluctuations of the atmospheric refractive index n along the direction r are described by the refractive index structure $D_n(r)$. For locally isotropic turbulence fields, the structure function of the velocity field can be written as

$$D_n(r) = C_n^2 r^{2/3} \qquad (1)$$

where C_n^2 is called the refractive index structure coefficient and can be considered a measure of the strength of turbulence. In Kolmogorov's formulation $l << r << L$, with l being the inner scale, or the size below which viscous effects are important and energy is dissipated into heat, and L is the outer scale or the size above which isotropic behavior is violated (Fig. 1). For eddies with sizes between the inner and outer scales, fluctuations in the refractive index are correlated. A detailed review of this formulation can be found in Tatarski (1961, 1971), Roddier (1981), and Vernin (2011). Astro-parameters of importance for ground-based astronomy can be derived once C_n^2 is known (Roddier 1981; Businger and Cherubini 2011). Among these parameters, seeing is defined as

$$\varepsilon = 0.98\frac{\lambda}{r_0}, \tag{2}$$

where

$$r_0 = \left[0.423\left(\frac{2\pi}{\lambda}\right)^2 \int_0^L C_n^2(z)dz\right]^{-3/5}. \tag{3}$$

Fluctuations in the refractive index are related to corresponding fluctuations in temperature, pressure, and humidity. At high altitude locations such as Mauna Kea, Hawaii, the humidity fluctuations account for less than 1% of the value of the index of refraction and pressure fluctuations are negligible. Therefore, the refractive index fluctuations associated with the visible and near-infrared region of the spectrum are caused primarily by random temperature fluctuations.

The statistical description of the random field of turbulence-induced fluctuations in the atmospheric refractive index is similar to that for the related velocity field fluctuations. The concept of a conservative passive addititve (passive scalar) allowed Obukhov (1949) to relate the velocity structure function to the structure function for the variations on the refractive index as follows:

$$C_n^2(z) = a^2\left(\frac{K_H}{K_M}\right)L_0^{4/3}M^2 \qquad (4)$$

where:

$$M = \frac{80\times10^{-6}\,p}{T^2}\left(\frac{\partial T}{\partial z}\right), \qquad (5)$$

L_0 is the turbulent mixing length that characterizes the turbulent eddies, K_H and K_M are the exchange coefficients for heat and momentum, and a is an empirical constant.

The refractive index structure and the temperature structure, for most astronomical purposes, are related by the (Gossard, 1977)

$$C_n^2(z) = \left(\frac{80\times10^{-6}\,p}{T^2}\right)^2 C_T^2(z)\,. \qquad (6)$$

Tatarski (1961, 1971) pointed out that temperature is not a conservative passive additive and defines a pseudo-potential temperature as

$$H = T + \gamma_a z\,, \qquad (7)$$

which is an approximation of the potential temperature under conditions of hydrostatic equilibrium, where $\gamma_a = g/c_p$. He then derives an alternative formulation for M, which takes into account the fact that in the free atmosphere (i.e., above the ground layer), the adiabatic lapse rate γ_a could be comparable to the environmental temperature gradient

$$M = \frac{80\times10^{-6}\,p}{T^2}\left(\frac{\partial T}{\partial z} + \gamma_a\right). \qquad (8)$$

The derivation of (8) in Tatarski (1961, 1971) assumes that the atmosphere is in hydrostatic equilibrium and that the temperature change of a displaced parcel will follow an adiabatic lapse rate. Tatarski (1971) pointed out that this formulation is not valid for temperature fluctuations associated with larger vertical air motions. H is obtained by expanding θ in series and using the barometric equation, and this approximation is most valid in the lower troposphere.

Tatarski and others have referred to H as a "potential temperature", which has led some authors to substitute θ for H in the structure function, thus writing C_θ^2 instead of the C_T^2 for the temperature structure function in (6), and the following is found often in the literature

$$C_n^2(z) = \left(\frac{80 \times 10^{-6} p}{T^2} \right)^2 C_\vartheta^2(z). \tag{9}$$

As a result there is a lack of clarity in the literature regarding the derivation of C_n^2 and what formulation of the refractive index structure function is best suited for which application. The goal of this note is to shed light on these issues. In particular, we demonstrate that application of Tatarski's formulation results in increasing errors aloft, which may impact calculation of C_n^2 and seeing above the lower troposphere.

2. Another Look at the Refractive Index Structure Function

Following Tatarski (1971), an analytical expression for C_n^2 is derived in this section from basic principles, using the potential temperature θ instead of H. For application with electromagnetic waves, the refractive index n can be expressed as follows

$$n - 1 = \frac{80 \cdot 10^{-6}}{T} \left(p + \frac{4800 e}{T} \right), \tag{10}$$

where T is temperature (K), p is pressure (mb), and e is water vapor pressure (mb). Because T and e are not conservative additives, (10) can best be expressed as a function of the potential temperature θ and the specific humidity q, which are both conservative variables. The potential temperature is defined as

$$\vartheta = T\left(\frac{p_0}{p}\right)^{R/C_v} \tag{11}$$

where p_0 is the reference pressure at 1000 mb, R is the ideal gas constant, and C_v is the heat capacity at constant volume. The specific humidity is defined by

$$e = 1.62pq. \tag{12}$$

Expression (10) expressed in terms of θ and e becomes

$$(n-1)\cdot 10^{-6} = N = \frac{80p}{\vartheta\left(p_0/p\right)^{R/C_v}}\left(p + \frac{4800\times 1.62pq}{\vartheta\left(p_0/p\right)^{R/C_v}}\right) \tag{13}$$

that is $N=N(z, p(z), \theta(z), q(z))$.

For example, suppose a parcel of air raises from height z_1 to z_2. The value of N for this parcel will undergo the following

$$N_1=N(z_1, p(z_1), \theta(z_1), q(z_1)) \Rightarrow N'=N(z_2, p(z_2), \theta(z_1), q(z_1))$$

with θ and q conserving their values. Therefore the variation of the refractivity at level z_2 between the environment and the raised parcel is

$$\Delta N = N(z_2,p(z_2),\vartheta(z_2),q(z_2)) - N(z_2,p(z_2),\vartheta(z_1),q(z_1)) \approx \left(\frac{\partial N}{\partial\vartheta}\frac{d\vartheta}{dz} + \frac{\partial N}{\partial q}\frac{dq}{dz}\right)\Delta z\,. \tag{14}$$

By applying (14) to (13) the following expression is found

$$\frac{\Delta n}{\Delta z} = -\frac{80p}{\vartheta^2\left(p_0/p\right)^{R/C_v}}\left[\left(1+\frac{2\times 4800\times 1.62q}{\vartheta\left(p_0/p\right)^{R/C_v}}\right)\frac{d\vartheta}{dz} - \frac{(4800\times 1.62)}{\left(p_0/p\right)^{R/C_v}}\frac{dq}{dz}\right]\cdot 10^{-6}. \tag{15}$$

Using the potential temperature definition (15) becomes

$$M = \frac{\Delta n}{\Delta z} = -\frac{80\cdot 10^{-6} p}{T\vartheta}\left[\left(1+\frac{2\times 4800\times 1.62q}{T}\right)\frac{d\vartheta}{dz} - \frac{(4800\times 1.62)}{T/\vartheta}\frac{dq}{dz}\right]. \qquad (16)$$

Under conditions where the contribution from moisture can be neglected, which is for most astronomical applications in the visible range, and following Tatarski's formalism, (16) becomes

$$M = -\frac{80\cdot 10^{-6} p}{T\vartheta}\left(\frac{d\vartheta}{dz}\right). \qquad (17)$$

This differs from (8) because of the presence in the denominator of the potential temperature and the use of potential temperature in the derivative not the approximate form *H*. Accordingly, the expression for C_n^2 becomes

$$C_n^2(z) = \left(\frac{80\times 10^{-6} p}{T\vartheta}\right)^2 C_\vartheta^2(z) \quad , \qquad (18)$$

where

$$C_\vartheta^2(z) = a^2\left(\frac{K_H}{K_M}\right)L_0^{4/3}M^2 \, . \qquad (19)$$

Equation (18) provides the true constant structure function for the potential temperature. No approximations were needed in its derivation. The next two sections will show the difference between *H* and ϑ and the possible impact that using one versus the other might have in the estimation of optical turbulence.

2.1 Evaluating the Difference between H and ϑ

A sample plot of *H* and ϑ as a function of height shows that *H* is a good approximation for ϑ for most of the atmosphere below the temperature inversion at an altitude of ~2 km (Fig. 2, 3). However, the values of H and ϑ start to differ significantly at about 6-7 kilometers above sea level; consequently their derivatives will also differ.

Current weather models that include algorithms to model optical turbulence extend well into the stratosphere. For these applications, ϑ is the better choice of conservative variable to use in these algorithms. The results from a case study of the impact of using one formulation versus the other in model calculations are presented in the next section.

3. Numerical Model Application of the New Formulation

The model used in this study is the Weather Reaserch and Forecasting (WRF) model (Klemp et al. 2007, http://www.wrf-model.org). The model configuration chosen for this case study is the same operational configuration used at the Mauna Kea Weather Center (MKWC, http://mkwc.ifa.hawaii.edu; Businger et al. 2002). The configuration of WRF is the same as detailed in Cherubini et al (2011) and the nested domains are shown in Fig. 4. The WRF model is initialized with the National Centers for Environmental Prediction (NCEP) Global Forecasting System (GFS) analyses. Boundary conditions are updated every 6 hours also using the GFS analyses[1].

In this implementation, the optical turbulence algorithm is parameterized following equations (17), (18), and (19). The exchange coefficients for heat and momentum, K_H and K_M, are parameterized within the model planetary boundary layer

[1] Using the GFS analyses instead of the GFS forecasts, as it is usually done in an operational setting, helps to reduce the impact of forecast error.

scheme (Mellor-Yamada-Janjic scheme, Janjic, 2002), while the outer length scale of turbulence is parameterized as described in Masciadri et al (1999). The full details regarding the optical turbulence algorithm are not included here for the sake of brevity and can be found in Cherubini et al (2011)

As proposed by Masciadri and Jabouille (2001), and Masciadri et al. (2004), in order for turbulent production to begin under conditions of a stable atmosphere, the turbulent scheme requires a non-zero background for the Turbulent Kinetic Energy (TKE). Within the WRF MYJ boundary layer scheme, which solves the TKE budget equation, the background TKE is set to E_{min}= 0.1 $m^2 s^{-2}$. For optical turbulence purposes though, this value is too large to produce realistic values of C_n^2 profiles in the upper troposphere. In this work the background TKE is set to $E_{min}= 1 \cdot 10^{-4}\ m^2 s^{-2}$. In practice, a calibration of E_{min} based on observations is recommended. The calibration allows the determination of a set of E_{min} values as a function of the different layers/profiles of the atmosphere, and therefore, of the characteristics of each turbulence region. Details on the calibration used in this experiment can be found in Cherubini et al (2011).

3.1 Case Study from the 2002 Campaign

The vertical distribution of turbulence over Mauna Kea was measured as a part of a site characterization campaign held during October and December 2002. For the purpose of this work, only the data from the Generalized SCIntillation Detection And Ranging (G-SCIDAR) for the October portion of the campaign are used. For more details on the G-SCIDAR and it was operated during the 2002 MK campaign, the reader can refer to Cherubini et al. (2008).

Once the algorithm to calculate C_n^2 and seeing was revised in the WRF code as indicated in section 4.1, the model was rerun for the 23 October 2002. WRF was initialized at 0000 UTC of that same nominal day. Optical turbulence profiles from the G-SCIDAR collected between 0600 UTC (2000 HST) and 1600 UTC (0400 HST) were considered and compared to the WRF output valid during the same timeframe. The C_n^2 simulated data are from the WRF innermost domain, with horizontal resolution of 1 km. Although the implemented algorithm produces C_n^2 in the surface layer, only simulated data from 70 m and up have been used in the comparison to match the G-SCIDAR observation range. Figure 5 shows a comparison of two WRF runs to show the impact of the C_n^2 formulation, i.e., whether equations (9) or (18) is used to calculate C_n^2. The comparison illustrates how, as expected, the differences among the C_n^2 profiles increase with height given the intrinsic differences between T and θ and given the differences, already described in section 3, between H and θ.

Clearly, the choice of the denominator in the C_n^2 definition has an appreciable impact on the simulated C_n^2 profiles. The two formulations of C_n^2 provide same vertical profile shape, but different inclinations/intensities. The analytical derivation in section 2, free of approximations, suggests that the correct formulation is provided by equations (17) and (18). No calibration is included in the results shown in Fig. 5, because a discussion of calibration is beyond the scope of this note.

The optical turbulence algorithm implemented in the current version of the operational WRF model running at the MKWC includes these latest findings. A good agreement between observed and predicted seeing is seen in Fig. 6. In this particular case, the WRF algorithm was able to capture not only the average nightly seeing value but also the variability through the night.

4. Conclusions and Discussion

A review of the derivation of the refractive index structure function C_n^2 is provided in this paper to address a perceived lack of clarity in the literature regarding this topic. In this paper, C_n^2 has been derived following Tatarski (1971), but unlike in Tatarski (1971), the potential temperature ϑ is used as the passive conservative variable instead of the pseudo-potential temperature $H=T+\gamma_a$, which presumes that the atmosphere is in hydrostatic equilibrium. The difference between H and ϑ is illustrated through an example in section 3. Results from a sample case study show a positive impact for the upper troposphere when using the newer formulation of C_n^2 (Eq. 18) versus the traditional formulation (Eq. 9) in an optical turbulence algorithm implemented in the WRF model. The case study improved the agreement between observation and the synthetic C_n^2 profiles. The new formulation of C_n^2 may have applications in observational work to measure and seeing C_n^2.

Work to construct a robust calibration of the revised optical turbulence algorithm is currently in progress. The use of the MASS/DIMM system data, which has been operating at the summit of Mauna Kea since September 2009, and the Thirty Meter Telescope site monitoring campaign data will allow an accurate calibration based on data from a large sample of nights to more completely represent the range of turbulence conditions associated with the naturally occurring atmospheric variability. It may be interesting to investigate whether measurements of optical turbulence by traditional instruments (DIMM, MASS, and G-Scidar) that rely on equation (18) may also be affected by use of the new formulation in equation (9).

5. Acknowledgments

We would like to thank Rene' Racine for his constructive comments on an early draft. We would also like to thank Elena Masciadri for insightful discussion on this subject and comments on an early draft. This paper is IFA contribution no. xxxx.

6. References

Businger, S., R. McLaren, R. Ogasawara, D. Simons, and R. J. Wainscoat, 2002: Starcasting. *Bull. Amer. Meteor. Soc.*, **83**, 858–871.

Cherubini T., S. Businger and R. Lyman, 2011: *Seeing Clearly. The impact of Atmospheric Turbulence on the Propagation of Extraterrestrial Radiation*. S. Businger and T. Cherubini, Ed., VBW Publishing. 198 pp**.**

Cherubini, T., S. Businger, R. Lyman and M. Chun, 2008 a): Modeling turbulence and seeing over Mauna Kea. *J. Appl. Meteo.* **47**, 1140-1155.

Gossard E. E, 1977: Refractive index variance and its height distribution in different air masses. *Radio Science*, **12**, 89-105.

Janjic, Z. I., 2002: Nonsingular Implementation of the Mellor–Yamada Level 2.5 Scheme in the NCEP Meso model, NCEP Office Note, No. 437, 61 pp.

Klemp, J. B., W. C. Skamarock, and J. Dudhia, 2007: Conservative split-explicit time integration methods for the compressible nonhydrostatic equations. Mon. Wea. Rev.,

135, 2897-2913.

Kolmogorov, A. N., 1941: Local structure of turbulence in an incompressible viscous fluid at very large Reynolds numbers. *Comptes Rendus (Doklady) de l'Acadèmie des Sciences de l'U.R.S.S.*, **30**, 301-305. Translated in *Turbulence. Classic Papers on Statistical Theory*, editors: S. K. Friedlander and L. Topper. Interscience Publishers Inc., New York, 1961.

Masciadri, E., J. Vernin, and P. Bougeault, 1999: 3d mapping of optical turbulence using an atmospheric numerical model. i: a useful tool for the ground-based astronomy. *Astron. Astrophys. Supplement Series*, **137**, 185-202.

Masciadri, E., and J. P. Jabouille, 2001: Improvements in the optical turbulence parameterization for 3d simulations in a region around a telescope. *Astron. Astrophys.*, **376**, 727–734.

Masciadri, E., R. Avila, and L. Sánchez, 2004: Statistic reliability of the Meso-NH atmospherical model for 3D C_n^2 simulations. *Revista Mexicana de Astronomía y Astrofisíca*, **40**, 3-14.

Obukhov, A. M., 1949: Structure of the temperature field in a turbulent flow (in Russian). *Izv. Akad. Nauk SSSR Ser. Geogr. i Geopfiz*, **13**, 58–69.

Roddier, F., 1981: The effect of atmospheric turbulence in optical astronomy. *Progress in Optics*, **XIX**, 281–377.

Tatarski V.I., 1961: Wave Propagation in a turbulent Medium, McGraw-Hill.

Tatarski V.I. 1971: The Effects of the turbulent Atmosphere on Wave Propagation (translated from Russian by the Israel Program for Scientific Translations Ltd, ISBN 0 7065 0680 4) reproduced by National Technical Information Service, U.S.

Department of Commerce, Springfield, Va. 22151.

Vernin J., 2011: *Seeing Clearly. The impact of Atmospheric Turbulence on the Propagation of Extraterrestrial Radiation*. S. Businger and T. Cherubini, Ed., *VBW Publishing*. 198 pp.

List of Figures

Fig. 1 Schematic illustration of turbulent cascade process, with the energy input region, inertial subrange, and energy dissipation region where energy is dissipated as heat. *K* is the spatial wave number and *L* is the eddy size.

Fig. 2 Skew *T* diagrams for Hilo, HI at 12 UTC on 23 Oct 2002.

Fig. 3 Temperature (red line), potential temperature (blue line), and pseudo-potential temperature as defined in equation (11) (green line) calculated from the Hilo, HI, sounding at 12 UTC on 23 October 2002. For reference the dashed line on the left panel indicates Mauna Kea's summit level. The right panel shows more detail from the summit altitude to 20 km above sea level.

Fig. 4 MKWC configuration of the nested grids in WRF. Inset map shows an expanded view of the main island in the Hawaiian chain. The vertical resolution of the model is depicted in the diagram at right, including an expansion of the lowest 1200 meters of the model domain.

Fig. 5 Averaged nightly C_n^2 profile for 23 October 2002 as observed (black dashed line) and predicted by the WRF algorithm when T^2 (gray solid line) and $T\theta$ (black solid line) are used respectively in the definition of C_n^2.

Fig. 6 Observed MASS (blue dots) and DIMM (red dots) seeing for the night from 1800 HST 24 October 2011 to 0600 HST on 25 October 2011. The gray solid line is the WRF predicted seeing from the operational WRF run.

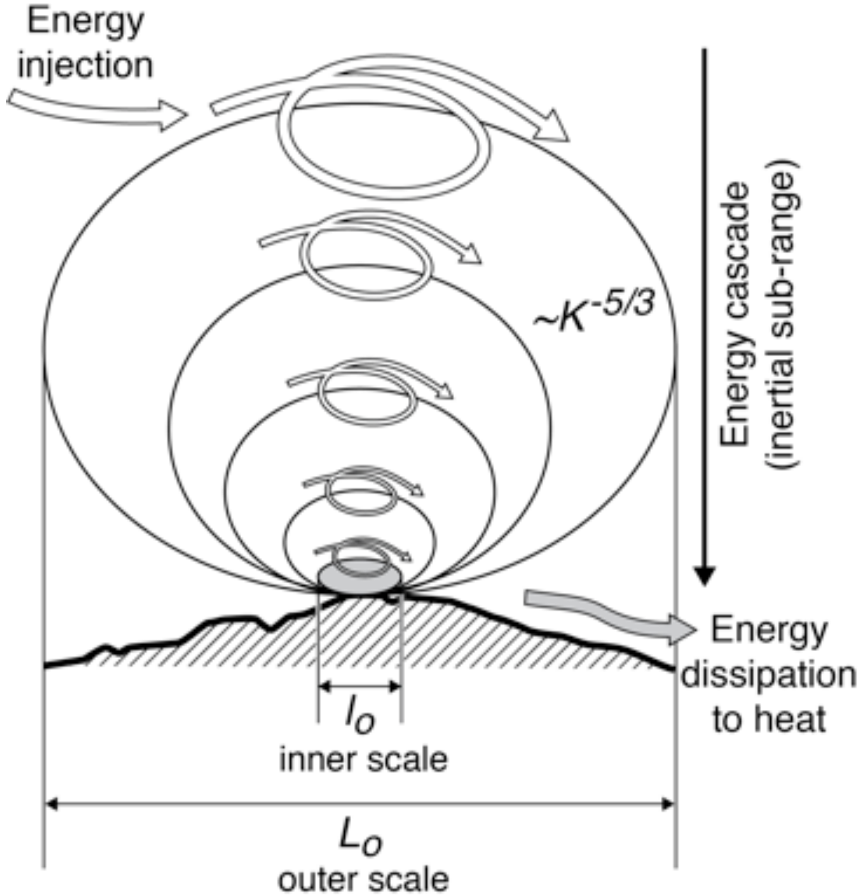

Fig. 1 Schematic illustration of turbulent cascade process with the energy input region, inertial subrange, and energy dissipation region where energy is dissipated as heat. *K* is the spatial wave number and *L* is the eddy size.

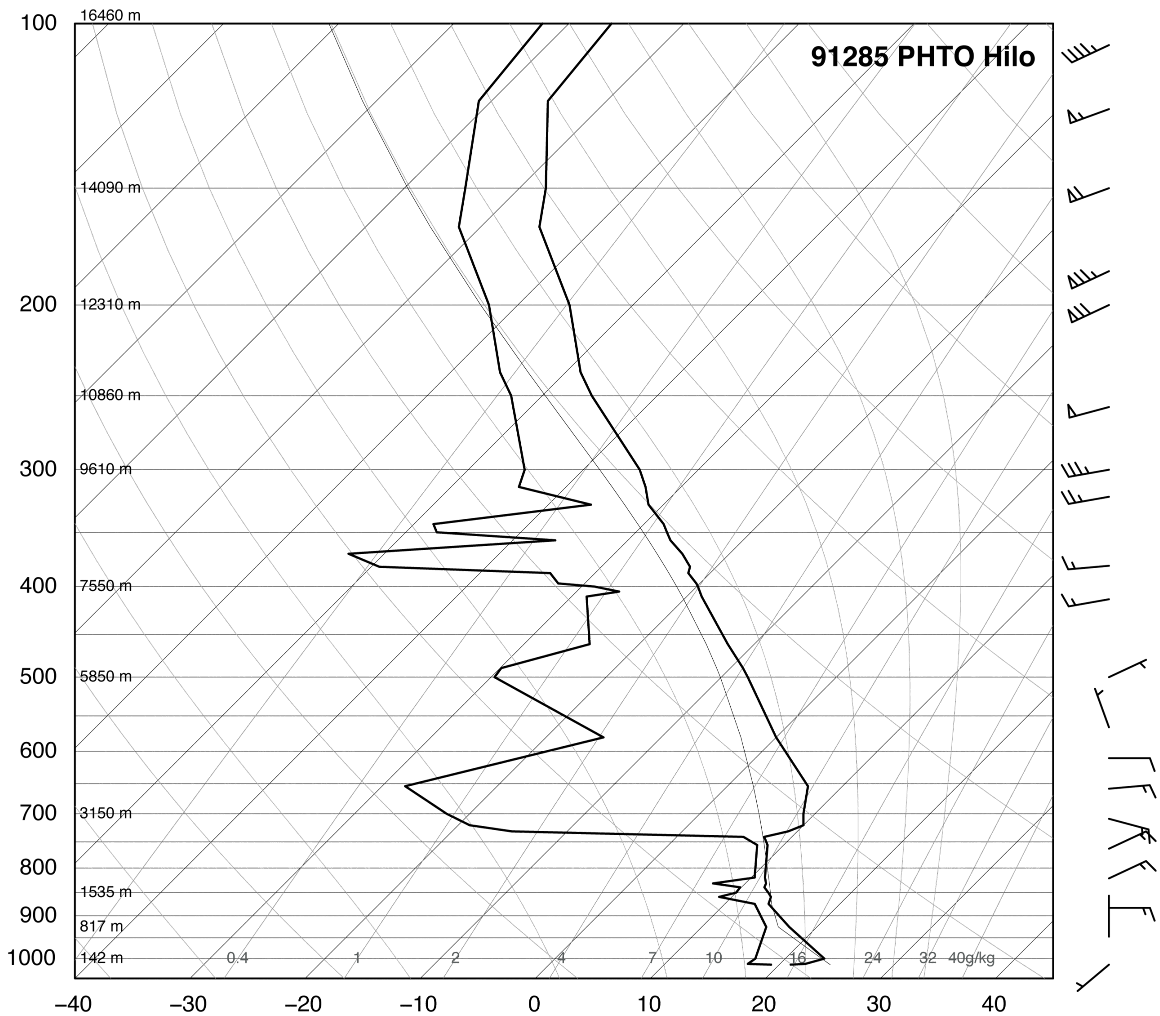

Fig. 2 Skew *T* diagrams for Hilo, HI at 12 UTC on 23 Oct 2002.

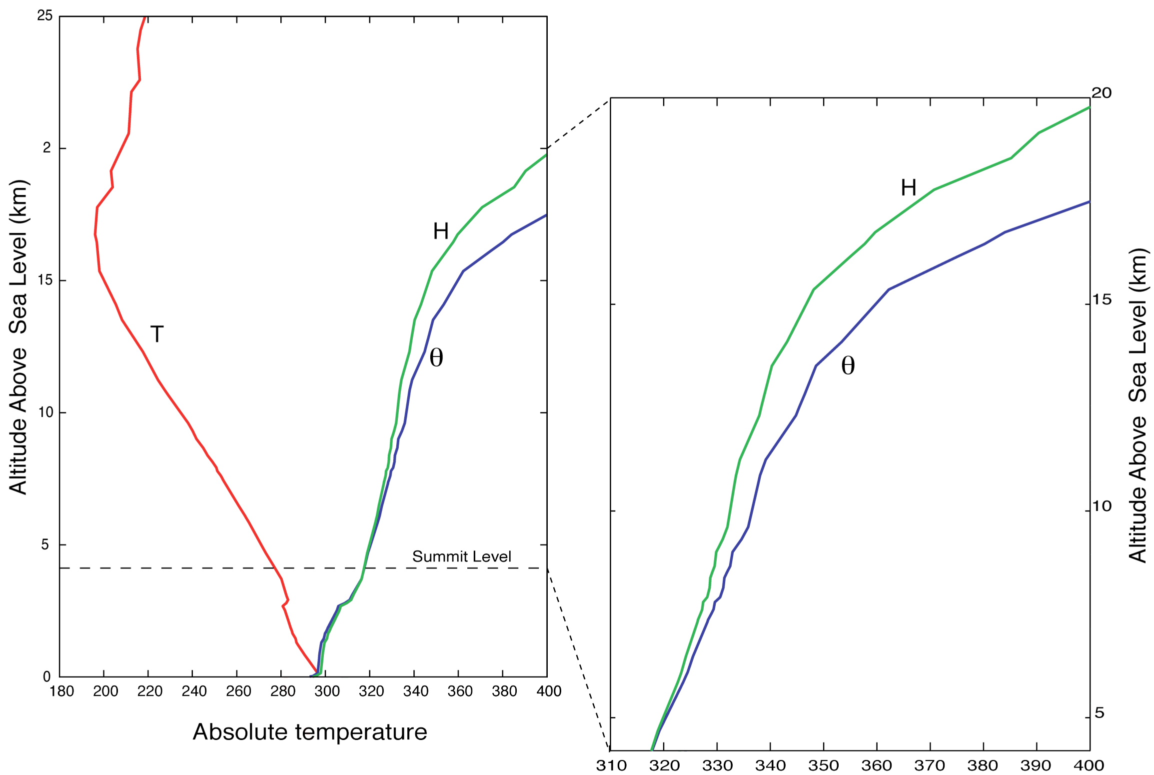

Fig. 3 Temperature (red line), potential temperature (blue line), and pseudo-potential temperature as defined in equation (11) (green line) calculated from the Hilo, HI, sounding at 12 UTC on 23 October 2002. For reference the dashed line on the left panel indicates Mauna Kea's summit level. The right panel shows more detail from the summit altitude to 20 km above sea level.

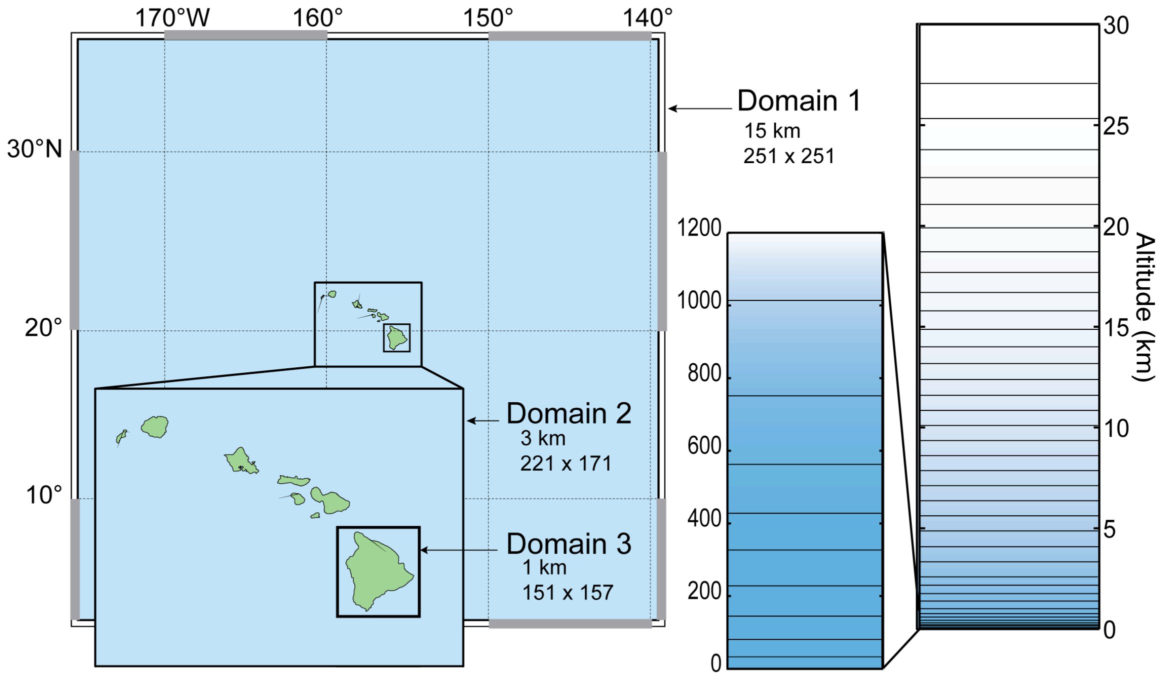

Fig. 4 MKWC configuration of the nested grids in WRF. Inset map shows an expanded view of the main island in the Hawaiian chain. The vertical resolution of the model is depicted in the diagram at right, including an expansion of the lowest 1200 meters of the model domain.

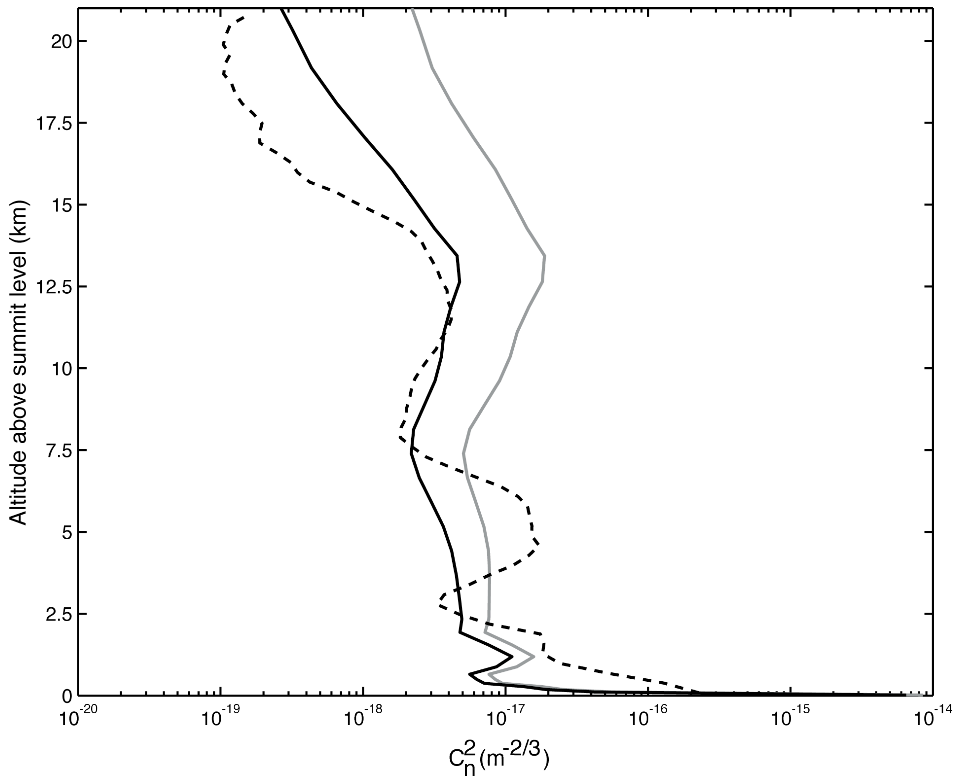

Fig. 5 Averaged nightly C_n^2 profile for 23 October 2002 as observed (black dashed line) and predicted by the WRF algorithm when T^2 (gray solid line) and $T\theta$ (black solid line) are used respectively in the definition of C_n^2.

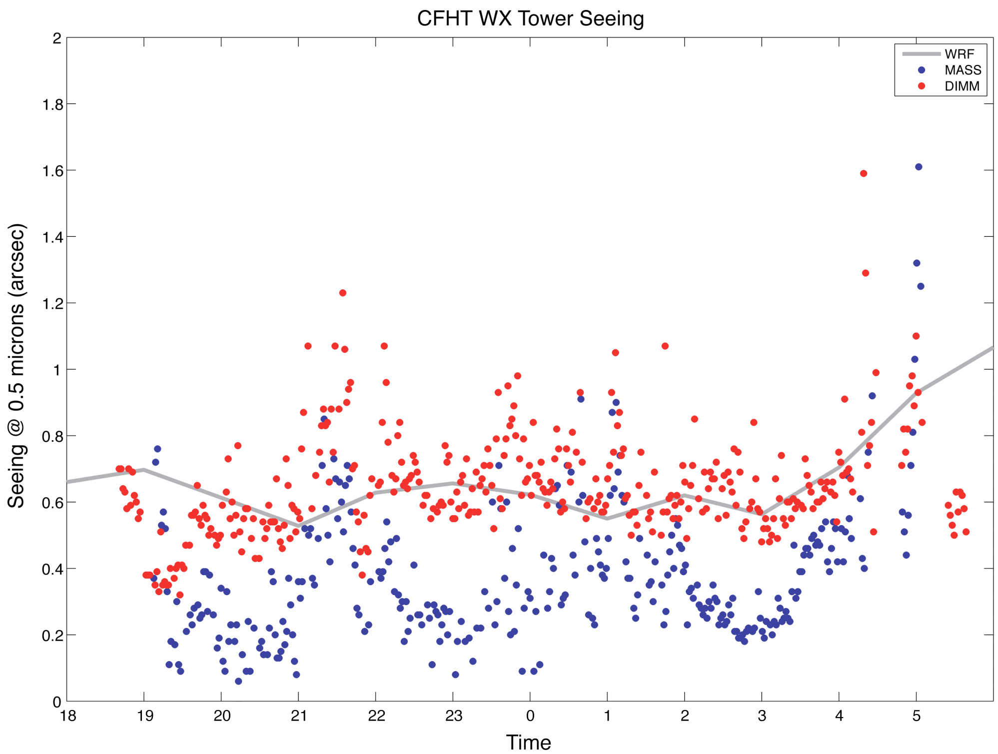

Fig. 6 Observed MASS (blue dots) and DIMM (red dots) seeing for the night from 1800 HST 27 October 2011 to 0600 HST on 28 October 2011. The gray solid line is the WRF predicted seeing from the operational WRF run.